

Two types of charge order in the superconducting kagome material CsV₃Sb₅

Ritu Gupta^{§,1,*} Debarchan Das^{§,1,†} Charles Mielke III,¹ Ethan Ritz,² Fabian Hotz,¹ Qiangwei Yin,³ Zhijun Tu,³ Chunsheng Gong,³ Hechang Lei,^{3,‡} Turan Birol,² Rafael M. Fernandes,⁴ Zurab Guguchia,¹ Hubertus Luetkens,^{1,§} and Rustem Khasanov^{1,¶}

¹Laboratory for Muon Spin Spectroscopy, Paul Scherrer Institute, CH-5232 Villigen PSI, Switzerland

²Department of Chemical Engineering and Materials Science, University of Minnesota, MN 55455, USA

³Department of Physics and Beijing Key Laboratory of Opto-electronic Functional Materials & Micro-nano Devices, Renmin University of China, Beijing 100872, China

⁴School of Physics and Astronomy, University of Minnesota, Minneapolis, MN 55455, USA

(Dated: March 11, 2022)

The kagome metals of the family AV₃Sb₅, featuring a unique structural motif, harbor an array of intriguing phenomena such as chiral charge order and superconductivity. CsV₃Sb₅ is of particular interest because it displays a double superconducting dome in the region of the temperature-pressure phase diagram where charge order is still present. However, the microscopic origin of such an unusual behavior remains an unsolved issue. Here, to address it, we combine high-pressure, low-temperature muon spin relaxation with first-principles calculations. We observe a pressure-induced three-fold enhancement of the superfluid density, which also displays a double peak feature, similar to the superconducting critical temperature. This leads to three distinct regions in the phase diagram, each of which features distinct slopes of the linear relation between superfluid density and the critical temperature. These results are attributed to a possible evolution of the charge order pattern from the superimposed tri-hexagonal Star-of-David phase at low pressures (within the first dome) to the staggered tri-hexagonal phase at intermediate pressures (between the first and second domes). Our findings suggest a change in the nature of the charge ordered state across the phase diagram of CsV₃Sb₅, with varying degrees of competition with superconductivity.

Among the series AV₃Sb₅ (A = Rb, K, Cs),¹⁻³ the Cs compound manifests the highest superconducting critical temperature $T_c \simeq 2.5$ K. CsV₃Sb₅ also features multi-gap superconductivity and more importantly, a time reversal symmetry breaking (TRSB) chiral charge order below $T_{co} = 94$ K,⁴⁻⁷ as reported by scanning tunneling microscopy,⁸ polar Kerr rotation,⁵ and μ SR experiments.^{4,6} A comprehensive understanding of the interdependence between charge order (CO) and superconductivity (SC) is thus essential, and can be studied by using an appropriate external perturbation. In the quest to obtain an efficient tuning knob, hydrostatic pressure was found to be optimal. Indeed, pressure suppresses the charge order and results into an unusual but well-pronounced double superconducting dome in the temperature-pressure phase diagram.

Compared to the Rb and K counterparts,⁹⁻¹¹ the double peak behavior is most distinguishable in the case of CsV₃Sb₅¹²⁻¹⁵ where T_c is roughly tripled to 8 K around the optimal pressure of 2 GPa from its value $T_c = 2.5$ K at ambient pressure. Thus, pressure tuned CsV₃Sb₅ offers a rich framework for studying the nature of the interplay between superconductivity and charge order.

To systematically characterize and to obtain a microscopic understanding of the complex temperature-pressure phase diagram of CsV₃Sb₅, here we report high-pressure zero-field and transverse-field μ SR as well as AC susceptibility (up to 1.75 GPa) measurements combined with first principles calculations. Transverse field (TF) μ SR experiments serve as an extremely sensitive local probe technique to measure the magnetic penetration depth λ in the vortex state of bulk type II superconductors. This quantity is directly related to the superfluid density n_s via $1/\lambda^2 = \mu_0 e^2 n_s / m^*$ (where m^* is the effective mass). Zero-field μ SR has the ability to detect internal magnetic fields as small as 0.1 G without applying external magnetic fields, making it a highly valuable tool for probing spontaneous magnetic fields due to TRSB in exotic superconductors. The techniques of μ SR and DFT complement each other ideally, as we are able to sensitively probe the fundamental microscopic properties of CsV₃Sb₅ with μ SR experiments and correlate them with the pressure-evolution of the charge ordered state calculated by DFT.

I. RESULTS

A. Superfluid density as a function of pressure

Figure 1(a) shows the TF- μ SR time spectra of CsV₃Sb₅ well below (0.25 K) and above (10 K) T_c in the presence of an applied magnetic field of 10 mT for ambient as well as the highest applied pressure, 1.74 GPa. The weakly damped oscillations above T_c are essentially due to the randomly distributed local fields created by nuclear magnetic moments. The spectra below T_c show a sizable increase in relaxation because of the inhomogeneous distribution of internal fields arising due to the formation of the flux line lattice in the vortex state. The Fourier transform of the spectra, shown in Fig.

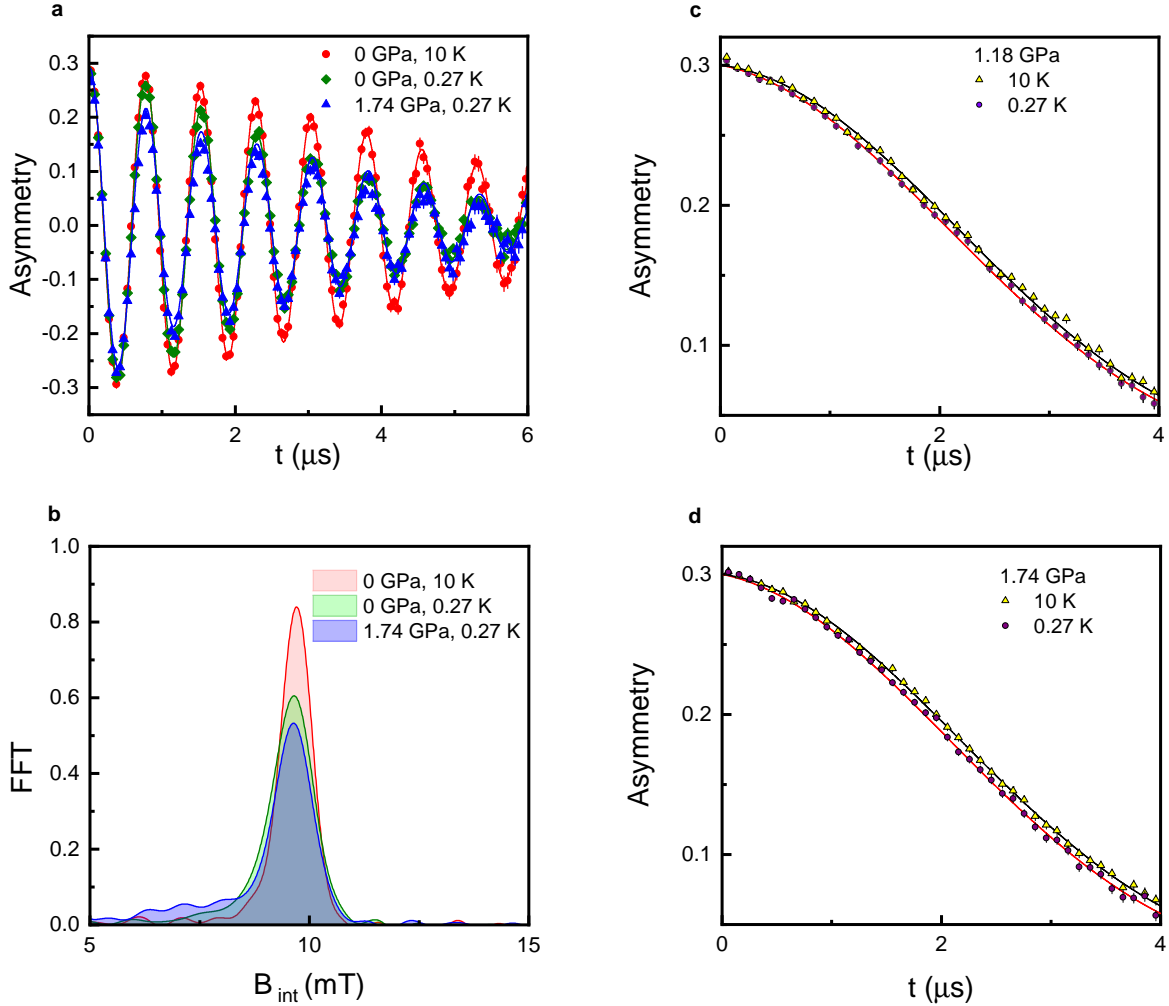


FIG. 1: (Color online) **TF and ZF- μ SR time spectra.** a.) Selected TF- μ SR time spectra at 0.27 K (in the superconducting state) and 10 K (in the normal state) collected for ambient and 1.74 GPa pressure. Solid lines are the fits of the spectra considering both the sample and background parts, as described in the Supplementary section. b.) The fast Fourier transform of the spectra shows an additional broadening of the peak due to an inhomogeneous distribution of internal fields, resulting from the appearance of a vortex lattice. c.)-d.) Representative ZF- μ SR time spectra collected in zero field well below T_c (0.27 K) and above T_c (10 K) for 1.18 GPa [panel (c)] and 1.74 GPa [panel (d)]. The solid lines are fits considering two relaxation channels, namely Gaussian-Kubo-Toyabe and a Lorentzian decay function.

1b, gives the internal field distribution, which showcases a clear broadening in the superconducting state compared to the normal state. From the TF- μ SR data, the superconducting relaxation rate $\sigma_{sc}(T)$ is extracted. The latter is related to the magnetic penetration depth via $\frac{\sigma_{sc}(T)}{\gamma_\mu} = 0.06091 \frac{\phi_0}{\lambda^2(T)}$, where $\gamma_\mu = 2\pi \times 135.5$ MHz/T is the muon gyromagnetic ratio and ϕ_0 is the flux quanta^{16,17} (details of the analysis of the TF- μ SR data are given in the Supplementary section). The resulting temperature dependence of the inverse squared magnetic penetration depth $\lambda^{-2}(T)$, measured under various hydrostatic pressures, are shown in Fig. 2(a).

The $\lambda^{-2}(T)$ curves in Fig. 2(a) are well described by a two-gap model across the entire pressure range probed (see details in the Methods section).

This indicates that the multi-gap nature of the superconducting state of CsV_3Sb_5 , which was previously reported by various techniques for ambient conditions,¹⁸⁻²¹ is robust against the application of hydrostatic pressure. As we show below, a sharp increase of both T_c and $\lambda^{-2}(0)$ occurs at pressures in the range 1.5 – 1.7 GPa, suggesting the complete suppression of the CO and thus a transition between the SC+CO state to the pure SC state. It is quite remarkable, therefore, that at the intermediate pressure 1.68 GPa, which is at the border between the SC+CO and pure SC phases, the temperature evolution of the penetration depth shows a prominent two-step like feature [purple curve in Fig. 2(a)]. This is a signature of inhomogeneity, whose origin can be either extrinsic, e.g., due to pressure inhomogeneity

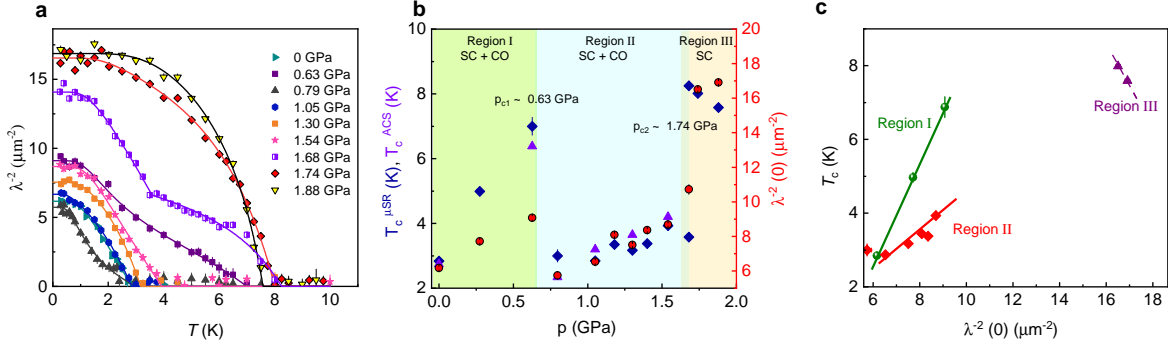


FIG. 2: (Color online) **Pressure dependence of the superconducting parameters and temperature-pressure phase diagram.** a.) Temperature variation of the inverse squared magnetic penetration depth $\lambda^{-2}(T)$ for the applied hydrostatic pressures shown in the plot legend. The solid line is a two gap $s + s$ -wave model fitting using the phenomenological α -model. b.) The temperature-pressure superconducting phase diagram of CsV_3Sb_5 . The left axis shows T_c values obtained through TF- μ SR and ac magnetic susceptibility measurements carried out under hydrostatic pressure conditions. The right axis presents the inverse squared London penetration depth at base temperature, i.e., $\lambda^{-2}(0) \propto n_s$ as a function of pressure. c.) Superconducting transition temperature T_c plotted as a function of the base-temperature superfluid density $\lambda^{-2}(0)$ for the three different regions of the phase diagram of panel (b).

inside the cell, or intrinsic, due to phase separation caused by a first-order SC+CO to SC transition.

Figure 2(b) shows the pressure dependence of T_c and of the zero-temperature value of $\lambda^{-2}(0)$, which is directly proportional to the superfluid density n_s . Interestingly, both $\lambda^{-2}(0)$ and T_c show a similar non-monotonic pressure dependence, featuring three distinct regions marked as I, II and III in Fig 2(b). Initially, as pressure increases, T_c shows an increase from 2.85(9) K at ambient pressure to 6.9(3) K at a critical pressure $p_{c1} \simeq 0.63$ GPa. Upon further increase in pressure, T_c shows a sharp and substantial decrease down to 2.87(7) K at 0.8 GPa. This marks the onset of Region II, where T_c increases only slightly with pressure. Remarkably, a sudden jump in T_c is seen around a second critical pressure $p_{c2} \simeq 1.74$ GPa, reaching a maximum value of $T_c^{\text{max}} = 8.0(1)$ K – which is almost three times larger than the ambient pressure value – and nearly saturating beyond this pressure. This regime is denoted as Region III in the $T - p$ phase diagram.

The maximum T_c value of 8 K extracted from μ SR is fairly close to the value obtained through electrical transport, AC and DC magnetization measurements.¹⁴ Moreover, $\lambda^{-2}(0)$ qualitatively shows a similar trend to T_c with regard to pressure, also featuring a double-peak behavior. Indeed, there is a nearly threefold increase in the value of $\lambda^{-2}(0)$ from 6.5(1) μm^{-2} at ambient pressure to 17.3(9) μm^{-2} at 1.74 GPa, followed by saturation upon further increase in pressure. The relative variation of the $\lambda^{-2}(0)$ value at the highest applied pressure compared to its ambient pressure value is $\delta\lambda^{-2}(0)/\lambda^{-2}(0) = 63\%$. This is rather unusual in comparison to BCS superconductors, where the superfluid density either depends weakly on pressure or remains pressure independent.²² The sudden enhancement of T_c and $\lambda^{-2}(0)$ has an intimate connec-

tion with the collapse of CO at the critical pressure p_{c2} , and is consistent with a first-order transition from the SC+CO phase to the pure SC phase.

B. Superconducting transition temperature vs. superfluid density

Figure 2(c) displays the correlation between the superconducting transition temperature T_c and the superfluid density $\lambda^{-2}(0)$ obtained from μ SR experiments under different pressures. There are three distinct types of $T_c(\lambda^{-2}(0))$ lines, each associated with one of the three regions of the phase diagram in Fig 2(b). For the data points belonging to Region I, we obtain a slope of 2.72 $\text{K}\mu\text{m}^2$, which is 3.5 times larger than the slope obtained for the data points from Region II (0.78 $\text{K}\mu\text{m}^2$). For Region III, $\lambda^{-2}(0)$ seems to be almost independent on T_c .

These linear relationships between T_c and $\lambda^{-2}(0)$ are characteristic of unconventional superconductors. In the present case, for Regions I and II, the $T_c/\lambda^{-2}(0)$ ratio lies far away from the values typically seen in BCS superconductors, where $T_c/\lambda^{-2} \approx 0.00025\text{--}0.015$ $\text{K}\mu\text{m}^2$. The large values of T_c , despite the small values of the superfluid density in Regions I and II, are also signatures of unconventional SC, where $T_c/\lambda^{-2}(0) \sim 1\text{--}20$.^{23–25} Moreover, the change in the slope $T_c/\lambda^{-2}(0)$ from Region I to Region II, both of which display coexisting CO and SC, suggests a subtle modification in the CO state. Combined with the sudden suppression in T_c and $\lambda^{-2}(0)$ upon crossing the Region I to Region II boundary in Fig. 2b, this provides strong evidence for a distinct competition between SC and CO in these two regions. Finally, the fact that $\lambda^{-2}(0)$ is nearly independent of T_c in Region III can be attributed to the absence of a competing CO state in this region.

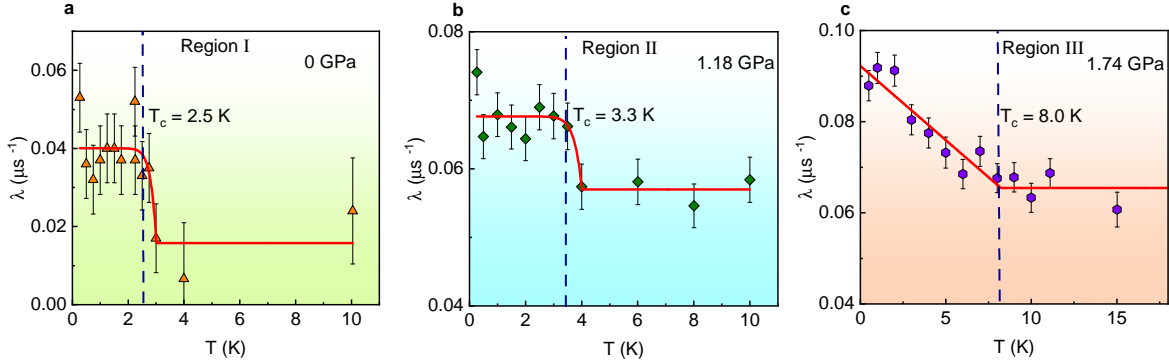


FIG. 3: (Color online) **Indication of time-reversal symmetry-breaking in the superconducting state of CsV_3Sb_5 .** a.) Electronic relaxation rate $\Lambda(T)$ for CsV_3Sb_5 as a function of temperature obtained from ZF- μ SR experiments carried out in the presence of three different applied pressures: (a) 0, (b) 1.18 and (c) 1.74 GPa. Each pressure corresponds to a different Region (I, II, and III) of the $T - p$ phase diagram of Fig. 2 (c). Solid lines through the data points are fits as described in the Methods section. The values for the superconducting transition temperature T_c are denoted by the vertical dashed black line.

C. Spontaneous fields in the superconducting state

Zero-field μ SR experiments have been successfully implemented to probe TRSB in well-known unconventional superconductors, e.g., Sr_2RuO_4 ,^{26–28} UPt_3 ,²⁹ LaNiC_2 ,³⁰ LaPt_3P .³¹ We have conducted ZF- μ SR experiments for three different applied pressures: 0, 1.18, and 1.74 GPa. Representative ZF- μ SR spectra above and below T_c for the pressures of 1.18 and 1.74 GPa are shown in Figs. 1(c) and (d). Both display an increase in relaxation within the superconducting state. The data were fitted using the Gaussian-Kubo-Toyabe (GKT) depolarization function³² multiplied by an exponential decay function $\exp(-\Lambda t)$. The Gaussian-Kubo-Toyabe function accounts for the random magnetic fields created by the nuclear moments. As was discussed previously for KV_3Sb_5 ,³ the exponential relaxation rate ($-\Lambda t$) is sensitive to the temperature dependence of the electronic contribution to the muon spin relaxation. The temperature dependences of the electronic relaxation rate $\Lambda(T)$ for the applied pressures of 0, 1.18 and 1.74 GPa are shown in Fig. 3.

At ambient pressure, we observe an enhancement of the exponential relaxation rate, with an onset slightly above T_c , by a small amount of $\Delta\Lambda_0 = 0.024(8) \mu\text{s}^{-1}$. Since time-reversal symmetry is already broken by charge order at $T_{\text{CO}} \simeq 95 \text{ K}$,^{4–6} we speculate that the effect in the superconducting state is caused by the Meissner screening of the small fields induced by the CO loop currents created at T_{CO} . A similar argument holds for 1.18 GPa (Region II), where both CO and SC coexist and the associated increase in electronic relaxation is $\Delta\Lambda_{1.18} = 0.011(2) \mu\text{s}^{-1}$.

However, at 1.74 GPa (Region III), where the CO is completely suppressed, we still observe an increase in $\Lambda(T)$ with the onset of SC at $T_c \simeq 8 \text{ K}$. The increase of $\Lambda(T)$ with decreasing temperature in

Region III is smooth, contrasting with the sharp increase observed in Regions I and II. As there is no CO at this pressure, a plausible origin for the enhancement of the internal field width is the spontaneous breaking of time reversal symmetry in the superconducting state. The increase in Λ by a magnitude of $\Delta\Lambda_{1.74 \text{ GPa}} = 0.031(3) \mu\text{s}^{-1}$ is associated with a characteristic field strength of $\Delta B = \Delta\Lambda_{1.74 \text{ GPa}}/\gamma_\mu = 0.04 \text{ mT}$. This value is comparable to what is observed in well-known TRSB superconductors, such as 0.05 mT for the chiral superconductor Sr_2RuO_4 ,^{27,28} 0.01 mT for the heavy-fermion superconductor UPt_3 ,²⁹ and 0.01 mT for the non-centrosymmetric superconductor LaNiC_2 .³⁰ These results indicate that the SC state without charge order breaks time-reversal symmetry. Interestingly, a recent μ SR investigation of the other kagome compounds, RbV_3Sb_5 and KV_3Sb_5 , also reported evidence for TRSB in the pure SC state.²⁴

II. DISCUSSION

One of the intriguing findings of this paper is the observation of a double superconducting dome inside the region where SC and CO coexist, associated with a more than threefold enhancement of T_c and of the superfluid density, $\sigma_{\text{sc}}(0) \propto n_s$. Indeed, Fig. 2(b) shows that with increasing pressure, T_c and the superfluid density first increase up to 0.63 GPa, followed by a sudden drop in these parameters with further increase in pressure, defining the boundary between Regions I and II. Within Region II, T_c and n_s increase slowly with increasing pressure up to 1.54 GPa, beyond which a dramatic enhancement is seen in these two quantities, marking the onset of Region III. This behavior is suggestive of a state of coexistence between competing SC and CO orders, which undergoes a transition to a pure SC state at p_{c2} . Such a scenario would naturally explain why not only T_c but also n_s displays a sudden change

from Region II to Region III, as n_s is suppressed in the coexisting state due to the partial gapping of the Fermi surface promoted by CO order.

Analogously, the strong variation of T_c and n_s between p_{c1} and p_{c2} is indicative of a subtle modification in the nature of either the CO or the SC state from Region I to Region II. The SC state seems qualitatively the same in both regions: first, the $\lambda^{-2}(T)$ curves are indicative of a fully-gapped SC state in both regions. Second, the temperature dependence of the electronic relaxation $\Lambda(T)$ is very similar in both Regions I and II (see Figs. 3(a) and 3(b)). Consequently, it is plausible that the changes in T_c and n_s are a consequence of a change in the CO state, in such a way that the CO of Region II competes more strongly with SC than the CO of Region I. Experimentally, it has been proposed that more than one CO state can be realized in these kagome metals.^{7,8,13} Different theoretical calculations also suggest multiple nearby CO instabilities.^{33–39} To investigate the possibility of a change in the nature of the CO state from Region I to Region II in CsV_3Sb_5 , we performed DFT calculations at different hydrostatic pressures.

The AV_3Sb_5 compounds are predicted to have phonon instabilities at the M and L points of their hexagonal Brillouin zones.^{40,41} Both of the unstable phonons transform as three-dimensional irreducible representations of the space group, which means that the high-temperature undistorted kagome lattice may lower its energy via lattice distortions along six independent atomic displacement patterns. Superpositions of these patterns give rise to a large family of candidate structures and bond order patterns, a subset of which are shown in Fig. 4.³⁷

While there is growing evidence of time-reversal symmetry breaking in the CO phase, the predominant effect of pressure is expected to be on the lattice, and not directly on the properties of the CO state affected by TRSB. This is because interatomic force constants depend strongly on the bond lengths in ionic compounds, where there is a fine balance between the repulsive and the attractive components of the interatomic interactions. Moreover, the TRSB CO state is generally expected to induce a regular (i.e. time-reversal symmetry preserving) CO pattern of bond distortions due to nonlinear terms in the free energy.^{36,39} For these reasons, despite the fact that our first-principles approach cannot directly account for TRSB, understanding how the crystal structure of CsV_3Sb_5 evolves under pressure using non-spin-polarized DFT calculations is a viable approach to elucidate the behavior of the CO in this material.

In Fig. 4(a), we present the enthalpy per formula unit of the three lowest energy CO structures of CsV_3Sb_5 calculated from DFT as a function of pressure. The parent structure, without CO, is shown in Fig. 4(d). Two of these CO phases, dubbed the $(M00) + (0LL)$ “staggered tri-hexagonal” state (red, pane (g)) and the $(MMM) + (LLL)$ “superimposed tri-hexagonal Star-of-David” phase (green, panel (f)), host a superposition of both M and L point lattice instabilities, and therefore have the $2 \times 2 \times 2$ pe-

riodicity consistent with the available X-ray data. The third low energy phase, the so-called (MMM) “planar tri-hexagonal” phase (blue, panel (e)), is only associated with the M point instability. As a result, it has a $2 \times 2 \times 1$ periodicity that seems inconsistent with the currently available experimental structure data.

Fig. 4(a) shows that at pressures above 5 GPa, CO is completely suppressed, and we predict the undistorted kagome lattice to be the equilibrium structure. This is consistent with previous results that predicted the phonon instabilities at both M and L to vanish at pressures between 3 GPa and 5 GPa.⁴² The threefold difference with respect to the experimental $p_{c,2}$ value is not unexpected. Indeed, an accurate prediction of the pressure at which the structural instabilities disappear is hard to achieve in DFT because of the large unit cell, the sensitivity of the electronic structure of the kagome layers on pressure, and lattice parameters errors due to the exchange correlation approximations. Nevertheless, the qualitative trends with pressure extracted from DFT are expected to be reliable.

While the staggered tri-hexagonal phase (red) has lower enthalpy than the other CO phases throughout the pressure range considered, the enthalpy differences between the distinct CO phases are on the order of a few meV’s per formula unit. This implies that entropic effects not captured by DFT are large enough to switch the ordering of these phases and cause the equilibrium structure to be a different phase from the one that minimizes the Kohn-Sham enthalpy. The two most likely candidates consistent with the experimentally observed $2 \times 2 \times 2$ periodicity of the CO state are the staggered tri-hexagonal (red) and the superimposed tri-hexagonal Star-of-David phases (green). Since the energy difference between these phases become smaller with increasing pressure, it is plausible that there is a transition from one to the other under pressure.

To elucidate which of these two CO phases is realized in Region I, we compute their densities of states (DOS). As shown in Fig. 4(b), there are important differences between the DOS curves of the staggered tri-hexagonal phase (red), the superimposed tri-hexagonal Star-of-David phase (green), and the undistorted kagome lattice (black). In particular, the latter has a larger DOS at the Fermi level, as well as van Hove singularities (signaled by the central “satellite” peaks in the DOS) closer to the Fermi level, when compared to the red and green curves (the blue curve, referring to the planar tri-hexagonal phase, is also shown for completeness). In contrast, the red curve has the smallest Fermi level DOS and farthest separated van Hove singularity peaks among the three curves. While the mechanism for superconductivity in CsV_3Sb_5 remains under debate, one generally expects that a higher Fermi-level DOS correlates with a higher T_c . Moreover, if van Hove singularities are important for the SC mechanism, it is reasonable to assume that the closer their peaks are to the Fermi level, the higher the T_c will

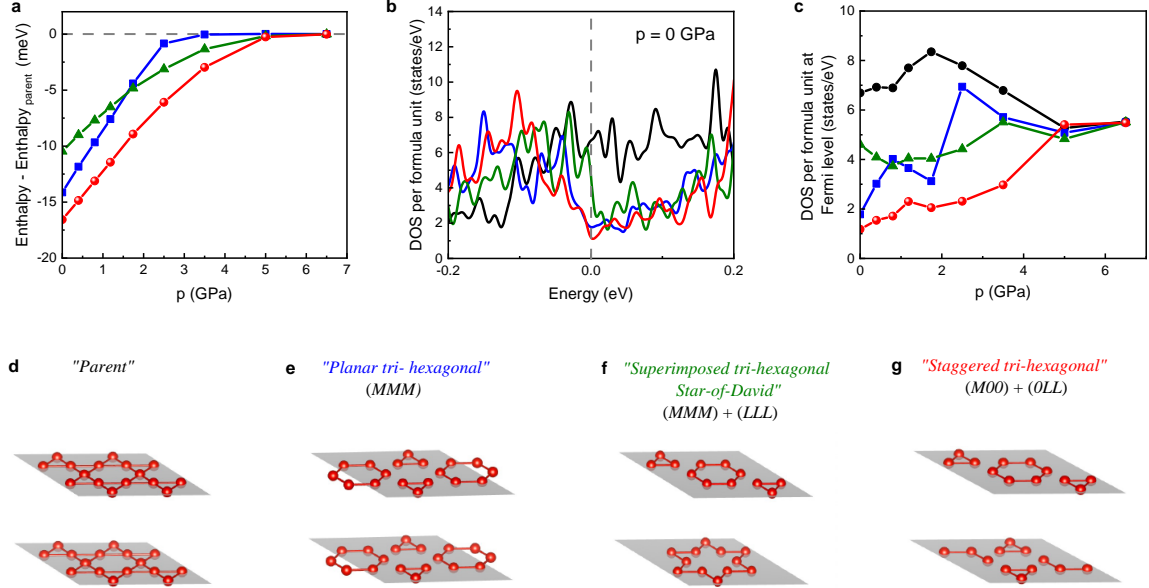


FIG. 4: (Color online) **Theoretical modeling and DFT results.** a.) Pressure dependence of the difference in enthalpies between a charge-ordered state and that of the undistorted kagome lattice for different possible CO phases discussed in the text and shown in panels (e)-(g). b.) Density of states (DOS) per formula unit calculated at ambient pressure for the different CO phases considered. c.) Variation of the DOS per formula unit at the Fermi level with pressure. The distinct types of CO states considered here display different bond order configurations and are named: d.) parent; e.) planar tri-hexagonal; f.) superimposed tri-hexagonal Star-of-David; and g.) staggered tri-hexagonal. Black, blue, green and red points in panels (a)-(c) correspond to these CO configurations respectively.

be. If these assumptions hold for CsV_3Sb_5 , then a possible explanation for the unusual double-peak SC dome revealed by our μSR data is a transition from the superimposed tri-hexagonal Star-of-David phase (green) in Region I to the staggered tri-hexagonal phase (red) in Region II. This is because the latter should compete more strongly with SC due to the larger reduction in the DOS and further separation between the van Hove peaks. Similarly, because the undistorted lattice (i.e. without CO) has the highest DOS, this would also account for T_c being the highest when all types of CO are suppressed at $p_{c,2}$.

III. CONCLUSION

Our results uncover two different regions in the part of the phase diagram of the kagome metal CsV_3Sb_5 where both charge order and superconductivity are present. Based on our DFT calculations, we propose that two distinct types of CO order are realized: a superimposed tri-hexagonal Star-of-David phase at low pressures and a staggered tri-hexagonal phase at intermediate pressures, before CO is fully suppressed. These charge orders display different degrees of competition with superconductivity, which leads to the complex phase diagram featuring a double-peak in the pressure dependence of both the superconducting transition temperature and the superfluid density. Throughout the pressure range investigated, the nodeless multigap nature of

the superconducting state remains persistent, in contrast to KV_3Sb_5 and RbV_3Sb_5 , where a nodal gap emerges at higher pressures.²⁴ Furthermore, we show that once charge order is fully suppressed, the superconducting state breaks time-reversal symmetry, which makes this compound, together with its K- and Rb-counterparts, one of the rare cases of unconventional superconductors with spontaneously broken time reversal symmetry.

IV. METHODS

Sample growth: Single crystals of CsV_3Sb_5 used for for this study were grown by using self-flux method from Cs ingots (purity 99.9%), V 3-N powder (purity 99.9%) and Sb grains (purity 99.999%).⁴³ The detailed description about the growth and characterization of crystals is provided in detail in Refs.^{20,44,45}

μSR experiment: Muon spin relaxation/rotation (μSR) measurements under pressure were performed at μE1 beam line using GPD spectrometer at Paul Scherrer Institute, Switzerland. This spectrometer is a dedicated worldwide unique instrument for carrying out high pressure μSR experiments. For μSR experiments, 100 % spin polarized muons μ^+ are implanted inside the sample one by one, where the spin of muon will Larmor precess around the local magnetic field B_{int} at the muon site. Detailed description about the μSR technique can be found in the Refs.^{46,47} In case of

a superconductor, the characteristic length scale namely penetration depth can be determined by probing the inhomogeneous field distribution of vortex lattice. Heliox cryostat with a He-3 insert was used to access temperature down to 250 mK. Pressure upto 1.9 GPa were achieved using low and pre-defined background double wall pressure cell made from MP35N/CuBe alloy, specifically designed for high pressure experiments.^{48,49} Single crystals of CsV₃Sb₅ were filled with random orientations inside the pressure cell in a compact cylindrical area of height 12 mm and diameter 6 mm. Daphne 7373 was used as a pressure medium to ensure the hydrostatic pressure conditions as it solidifies at much higher pressure ~ 2.5 GPa. Low temperature values of pressures were determined by tracking the superconducting transition of Indium, measured using ac susceptibility experiment. The fraction of muon stopping inside the sample was maximized to ~ 40 %.

We performed transverse-field (TF) and zero-field μ SR experiments at different pressures. Pressure cell is surrounded by four detectors: Forward, backward, left, and right with muon initial spin parallel to its momentum. The TF- μ SR experiments were performed in field cooled condition to get homogeneous vortex lattice formation. Approximately 10^6 positrons were recorded for each data point. The asymmetry vs. time spectra were analyzed using the open software package MUSRFIT.⁵⁰

Analysis of $\lambda(T)$: The temperature variation of magnetic penetration depth $\lambda^{-2}(T)$ is analyzed within the local (London) approach using following expression⁵¹:

$$\frac{\lambda^{-2}(T, \Delta_0)}{\lambda^{-2}(0, \Delta_0)} = 1 + \frac{1}{\pi} \int_0^{2\pi} \int_{\Delta(T, \phi)}^{\infty} \frac{\partial f}{\partial E} \frac{E dE d\phi}{\sqrt{E^2 - \Delta(T, \phi)^2}}$$

where $f = (1 + E/k_B T)^{-1}$ is the Fermi distribution function. The temperature and angular dependence of gap is given by $\Delta(T, \phi) = \Delta_0 \delta(T/T_c) g(\phi)$, where Δ_0 is the gap value at 0 K, $\delta(T/T_c) = \tanh\{1.821[1.018(T_c/T - 1)^{0.51}]\}$ represents the temperature dependence of gap. The angular dependence of the gap is represented by $g(\phi)$, which adapts a value 1 for isotropic s - wave model. We have fitted the $\lambda^{-2}(T)$ data at various pressures by separating it into two gaps:

$$\frac{\lambda^{-2}(T)}{\lambda^{-2}(0)} = x \frac{\lambda^{-2}(T, \Delta_{0,1})}{\lambda^{-2}(0, \Delta_{0,1})} + (1 - x) \frac{\lambda^{-2}(T, \Delta_{0,2})}{\lambda^{-2}(0, \Delta_{0,2})}. \quad (2)$$

In the above equation, x is the weight factor of the bigger gap $\Delta_{0,1}$. Fig. S3 shows the pressure dependence of the superconducting gaps ($\Delta_{0,1}$ and $\Delta_{0,2}$). In the regions where SC and CO coexists, i.e. Region I and II, fitting was done by considering the weight factor x as a global parameter for all pressures in the mentioned regimes. Similarly, for Region III, the fitting was done by assuming x as a global parameter in that region. The data at intermediate

pressure 1.68 GPa is fitted by considering a linear combination of Eq. 2 with parameter values fixed from that obtained for 1.54 GPa (corresponding to the SC+CO state) and 1.74 GPa (corresponding to the SC state).

Analysis of ZF relaxation rate: $\Lambda(T)$ at various pressures are fitted with following empirical relation:

$$\lambda(T) = \begin{cases} \Lambda_0, & T > T^* \\ \Lambda_0 + \Delta\Lambda \left[1 - \left(\frac{T}{T^*}\right)^n\right], & T < T^* \end{cases}. \quad (3)$$

where T^* is a characteristic temperature below which the increase in electronic relaxation starts. Λ_0 is the relaxation value above T_c , and $\Delta\Lambda$ is the change in relaxation after entering into the superconducting ground state. In Region I and II, the value of n is considerably high (14 and 15 respectively) indicating the step like increase in the relaxation rate. On the other hand, in Region III, where CO suppress completely, the value of n is 1 suggesting a linear increase in $\lambda(T)$ below T^* which coincides with T_c . As discussed in the main text, we conclude that in region III, T^* corresponds to the time reversal symmetry breaking transition T_{TRSB} .

DFT-calculations: All DFT calculations were performed using Projector Augmented Waves (PAW) as implemented in the Vienna Ab initio simulation package (VASP) version 5.4.4.⁵²⁻⁵⁴ We used the PBEsol exchange correlation functional, with valence configurations of $5s^2 5p^6 6s^1$, $3s^2 3p^6 3d^4 4s^1$, and $5s^2 5p^3$ corresponding to Cs, V, and Sb, respectively. Lattice parameters were found to be converged to within 0.001 Å using a plane wave cutoff energy of 450 eV, a Monkhorst-Pack k-point mesh of $20 \times 20 \times 10$ in the primitive cell, and a 2nd order Methfessel-Paxton smearing parameter of 10 meV.⁵⁵ Different phases have different specific volumes, and hence at finite pressure, the phase that minimizes the *enthalpy*, rather than the Kohn-Sham energy only, is the equilibrium structure at that volume.

Bilbao Crystallographic Server and tools therein were used for symmetry analysis of various theoretically obtained crystal structures.⁵⁶

Acknowledgments

We thank B. Andersen and M. Christensen for fruitful discussions. μ SR experiments were performed at the Swiss Muon Source (S μ S), Paul Scherrer Institute (PSI), Switzerland. H.C.L. was supported by National Key R&D Program of China (Grant No. 2018YFE0202600) and the Beijing Natural Science Foundation (Grant No. Z200005). T.B. and E.R. were supported by the NSF CAREER grant DMR-2046020. RMF (theory) was supported by the Air Force Office of Scientific Research under award number FA9550-21-1-0423.

Author contributions

R.G., D.D., C.M., Z.G., F. H., and R.K. performed μ SR experiments. R.G., D.D. and R.K. analyzed the μ SR data. Q.Y., Z.T., C.G., and H.C.L. synthesized and characterized samples. R. M. F., T. B., and E.R. performed the theoretical analysis. R. K. and H.L.

supervised the work at PSI. R.G., D.D., Z.G., and R. M. F. prepared the manuscript with notable inputs from all authors.

Competing interests

The authors declare no competing interests.

Data availability:

The data supporting the findings of this study are available within the paper and in the Supplementary Information. The raw data are available from the corresponding authors upon reasonable request.

- * Electronic address: ritu.gupta@psi.ch; Equal contribution
- † Electronic address: debarchandas.phy@gmail.com; Equal contribution
- ‡ Electronic address: hlei@ruc.edu.cn
- § Electronic address: hubertus.luetkens@psi.ch
- ¶ Electronic address: rustem.khasanov@psi.ch
- ¹ T. Neupert, M. Denner, J.-X. Yin, R. Thomale, and M. Hasan, *Nature Physics* **18**, 137 (2022).
 - ² K. Jiang, T. Wu, J.-X. Yin, Z. Wang, M. Hasan, S. Wilson, X. Chen, and J. Hu, arXiv preprint: arXiv:2109.10809 (2021).
 - ³ C. Mielke III, D. Das, J.-X. Yin, H. Liu, R. Gupta, Y.-X. Jiang, M. Medarde, X. Wu, H. Lei, et al., *Nature* **602**, 245 (2022).
 - ⁴ L. Yu, C. Wang, Y. Zhang, M. Sander, S. Ni, Z. Lu, S. Ma, Z. Wang, Z. Zhao, H. Chen, et al., arXiv preprint arXiv:2107.10714 (2021).
 - ⁵ Q. Wu, Z. Wang, Q. Liu, R. Li, S. Xu, Q. Yin, C. S. Gong, Z. Tu, H. C. Lei, T. Dong, et al., arXiv preprint: arXiv:2110.11306v2 (2021).
 - ⁶ R. Khasanov and et al., Under preparation (2022).
 - ⁷ Z. Wang, Y.-X. Jiang, J.-X. Yin, Y. Li, G.-Y. Wang, H.-L. Huang, S. Shao, J. Liu, P. Zhu, N. Shumiya, et al., *Physical Review B* **104**, 075148 (2021).
 - ⁸ H. Zhao, H. Li, B. R. Ortiz, S. M. L. Teicher, T. Park, M. Ye, Z. Wang, L. Balents, S. D. Wilson, and I. Zeljkovic, *Nature* **599**, 216–221 (2021).
 - ⁹ N. Wang, K. Chen, Q. Yin, Y. Ma, B. Pan, X. Yang, X. Ji, S. Wu, P. Shan, S. Xu, et al., *Physical Review Research* **3**, 043018 (2021).
 - ¹⁰ C. Zhu, X. Yang, W. Xia, Q. Yin, L. Wang, C. Zhao, D. Dai, C. Tu, B. Song, Z. Tao, et al., arXiv preprint arXiv:2104.14487 (2021).
 - ¹¹ F. Du, S. Luo, B. R. Ortiz, Y. Chen, W. Duan, D. Zhang, X. Lu, S. D. Wilson, Y. Song, and H. Yuan, *Physical Review B* **103**, L220504 (2021).
 - ¹² F. Yu, D. Ma, W. Zhuo, S. Liu, X. Wen, B. Lei, J. Ying, and X. Chen, *Nature communications* **12**, 1 (2021).
 - ¹³ Q. Wang, P. Kong, W. Shi, C. Pei, C. Wen, L. Gao, Y. Zhao, Q. Yin, Y. Wu, G. Li, et al., *Advanced Materials* **33**, 2102813 (2021).
 - ¹⁴ K. Chen, N. Wang, Q. Yin, Y. Gu, K. Jiang, Z. Tu, C. Gong, Y. Uwatoko, J. Sun, H. Lei, et al., *Physical Review Letters* **126**, 247001 (2021).
 - ¹⁵ Z. Zhang, Z. Chen, Y. Zhou, Y. Yuan, S. Wang, J. Wang, H. Yang, C. An, L. Zhang, X. Zhu, et al., *Physical Review B* **103**, 224513 (2021).
 - ¹⁶ E. Brandt, *Physical Review B* **37**, 2349 (1988).
 - ¹⁷ E. H. Brandt, *Physical Review B* **68**, 054506 (2003).
 - ¹⁸ H.-S. Xu, Y.-J. Yan, R. Yin, W. Xia, S. Fang, Z. Chen, Y. Li, W. Yang, Y. Guo, D.-L. Feng, et al. (2021).
 - ¹⁹ W. Duan, Z. Nie, S. Luo, F. Yu, B. R. Ortiz, L. Yin, H. Su, F. Du, A. Wang, Y. Chen, et al., arXiv preprint arXiv:2103.11796 (2021).
 - ²⁰ R. Gupta, D. Das, C. H. Mielke III, Z. Guguchia, T. Shiroka, C. Baines, M. Bartkowiak, H. Luetkens, R. Khasanov, Q. Yin, et al., arXiv preprint arXiv:2108.01574 (2021).
 - ²¹ K. Nakayama, Y. Li, T. Kato, M. Liu, Z. Wang, T. Takahashi, Y. Yao, and T. Sato, *Physical Review B* **104**, L161112 (2021).
 - ²² D. Das, R. Gupta, C. Baines, H. Luetkens, D. Kaczorowski, Z. Guguchia, and R. Khasanov, *Physical review letters* **127**, 217002 (2021).
 - ²³ Y. J. Uemura, G. M. Luke, B. J. Sternlieb, J. H. Brewer, J. F. Carolan, W. N. Hardy, R. Kadono, J. R. Kempton, R. F. Kiefl, S. R. Kreitzman, et al., *Phys. Rev. Lett.* **62**, 2317 (1989).
 - ²⁴ Z. Guguchia, C. Mielke III, D. Das, R. Gupta, J.-X. Yin, H. Liu, Q. Yin, M. Christensen, Z. Tu, C. Gong, et al., arXiv:2202.07713 (2022).
 - ²⁵ C. Mielke, Y. Qin, J.-X. Yin, H. Nakamura, D. Das, K. Guo, R. Khasanov, J. Chang, Z. Q. Wang, S. Jia, et al., *Phys. Rev. Materials* **5**, 034803 (2021).
 - ²⁶ G. M. Luke, Y. Fudamoto, K. Kojima, M. Larkin, J. Merrin, B. Nachumi, Y. Uemura, Y. Maeno, Z. Mao, Y. Mori, et al., *Nature* **394**, 558 (1998).
 - ²⁷ V. Grinenko, S. Ghosh, R. Sarkar, J.-C. Orain, A. Nikitin, M. Elender, D. Das, Z. Guguchia, F. Brückner, M. E. Barber, et al., *Nature Physics* **17**, 748 (2021).
 - ²⁸ V. Grinenko, D. Das, R. Gupta, B. Zinkl, N. Kikugawa, Y. Maeno, C. W. Hicks, H.-H. Klauss, M. Sigrist, and R. Khasanov, *Nature Communications* **12** (2021).
 - ²⁹ G. Luke, A. Keren, L. Le, W. Wu, Y. Uemura, D. Bonn, L. Taillefer, and J. Garrett, *Physical review letters* **71**, 1466 (1993).
 - ³⁰ A. D. Hillier, J. Quintanilla, and R. Cywinski, *Physical review letters* **102**, 117007 (2009).
 - ³¹ P. K. Biswas, S. K. Ghosh, J. Zhao, D. A. Mayoh, N. Zhigadlo, X. Xu, C. Baines, A. Hillier, G. Balakrishnan, and M. Lees, *Nature communications* **12**, 1 (2021).
 - ³² R. Kubo and T. Toyabe, North Holland, Amsterdam (1967).
 - ³³ N. Ratcliff, L. Hallett, B. R. Ortiz, S. D. Wilson, and J. W. Harter, arXiv preprint arXiv:2104.10138 (2021).
 - ³⁴ M. M. Denner, R. Thomale, and T. Neupert, *Physical Review Letters* **127** (2021).
 - ³⁵ X. Feng, K. Jiang, Z. Wang, and J. Hu, *Science Bulletin* (2021).
 - ³⁶ Y.-P. Lin and R. M. Nandkishore, *Phys. Rev. B* **104**, 045122 (2021).
 - ³⁷ M. H. Christensen, T. Birol, B. M. Andersen, and R. M. Fernandes, *Phys. Rev. B* **104**, 214513 (2021).
 - ³⁸ A. Subedi, *Phys. Rev. Materials* **6**, 015001 (2022).
 - ³⁹ T. Park, M. Ye, and L. Balents, *Phys. Rev. B* **104**, 035142 (2021).
 - ⁴⁰ S. Cho, H. Ma, W. Xia, Y. Yang, Z. Liu, Z. Huang, Z. Jiang, X. Lu, J. Liu, Z. Liu, et al., *Phys. Rev. Lett.* **127**, 236401 (2021).
 - ⁴¹ T. Qian, M. H. Christensen, C. Hu, A. Saha, B. M. Andersen, R. M. Fernandes, T. Birol, and N. Ni, *Phys. Rev. B* **104**, 144506 (2021).

- ⁴² J.-F. Zhang, K. Liu, and Z.-Y. Lu, Phys. Rev. B **104**, 195130 (2021).
- ⁴³ Q. Yin, Z. Tu, C. Gong, Y. Fu, S. Yan, and H. Lei, Chinese Physics Letters **38**, 037403 (2021).
- ⁴⁴ B. R. Ortiz, S. M. Teicher, Y. Hu, J. L. Zuo, P. M. Sarte, E. C. Schueller, A. M. Abeykoon, M. J. Krogstad, S. Rosenkranz, R. Osborn, et al., Physical Review Letters **125**, 247002 (2020).
- ⁴⁵ B. R. Ortiz, L. C. Gomes, J. R. Morey, M. Winiarski, M. Bordelon, J. S. Mangum, I. W. Oswald, J. A. Rodriguez-Rivera, J. R. Neilson, S. D. Wilson, et al., Physical Review Materials **3**, 094407 (2019).
- ⁴⁶ A. Yaouanc and P. D. De Reotier, *Muon spin rotation, relaxation, and resonance: applications to condensed matter*, vol. 147 (Oxford University Press, 2011).
- ⁴⁷ A. D. Hillier, S. Blundell, I. McKenzie, I. Umegaki, L. Shu, J. A. Wright, T. Prokscha, F. Bert, K. Shimomura, A. Berlie, et al., Nat. Rev. Method Primers **2**, 4 (2022).
- ⁴⁸ Z. Shermadini, R. Khasanov, M. Elender, G. Simutis, Z. Guguchia, K. Kamenev, and A. Amato, High Pressure Research **37**, 449 (2017).
- ⁴⁹ R. Khasanov, Z. Guguchia, A. Maisuradze, D. Andrica, M. Elender, A. Raselli, Z. Shermadini, T. Goko, F. Knecht, E. Morenzoni, et al., High Pressure Research **36**, 140 (2016).
- ⁵⁰ A. Suter and B. Wojek, Physics Procedia **30**, 69 (2012).
- ⁵¹ S. Serventi, G. Allodi, R. De Renzi, G. Guidi, L. Romano, P. Manfrinetti, A. Palenzona, C. Niedermayer, A. Amato, and C. Baines, Physical review letters **93**, 217003 (2004).
- ⁵² G. Kresse and J. Hafner, Phys. Rev. B **47**, 558 (1993).
- ⁵³ G. Kresse and J. Furthmüller, Comput. Mater. Sci. **6**, 15 (1996).
- ⁵⁴ G. Kresse and J. Furthmüller, Phys. Rev. B **54**, 11169 (1996).
- ⁵⁵ M. Methfessel and A. Paxton, Phys. Rev. B **40**, 3616 (1989).
- ⁵⁶ M. I. Aroyo, J. M. Perez-Mato, D. Orobengoa, E. Tasci, G. De La Flor, and A. Kirov, Bulgarian Chemical Communications **43**, 183 (2011), ISSN 08619808.

Two types of charge order in the superconducting kagome material CsV₃Sb₅

Ritu Gupta^{§,1,*} Debarchan Das^{§,1,†} Charles Mielke III,¹ Ethan Ritz,² Fabian Hotz,¹
Qiangwei Yin,³ Zhijun Tu,³ Chunsheng Gong,³ Hechang Lei,^{3,‡} Turan Birol,² Rafael
M. Fernandes,⁴ Zurab Guguchia,¹ Hubertus Luetkens,^{1,§} and Rustem Khasanov^{1,¶}

¹Laboratory for Muon Spin Spectroscopy, Paul Scherrer Institute, CH-5232 Villigen PSI, Switzerland

²Department of Chemical Engineering and Materials Science, University of Minnesota, MN 55455, USA

³Department of Physics and Beijing Key Laboratory of Opto-electronic Functional Materials & Micro-nano Devices,
Renmin University of China, Beijing 100872, China

⁴School of Physics and Astronomy, University of Minnesota, Minneapolis, MN 55455, USA

(Dated: March 11, 2022)

SUPPLEMENTARY INFORMATION

A. Alternating magnetic susceptibility under pressure

AC susceptibility (ACS) measurements under pressure were carried out to study the evolution of the superconducting transition temperature T_c with pressure. Additionally, the T_c of pure indium was also tracked for the estimation of the exact pressure inside the pressure cell at low temperature. The ACS curves collected at various pressures are shown in Fig. S1. T_c of the sample is taken as the point at which two straight lines extrapolated from the normal and superconducting states cross, whereas T_c of the indium is taken as the midpoint of the transition.

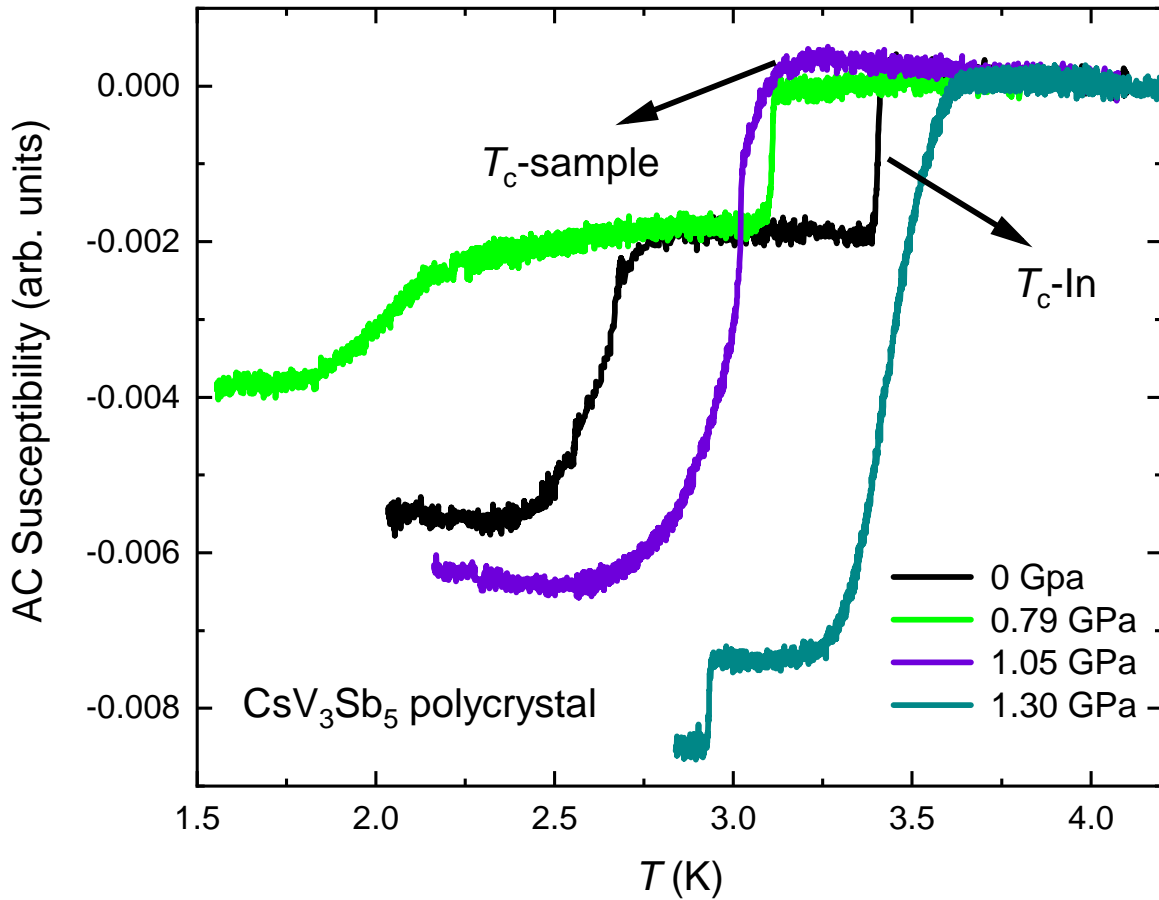


FIG. S1: A few selected ac magnetic susceptibility curves for CsV₃Sb₅ measured at ambient and various pressures. Arrows mark the position of the superconducting transition temperature for the sample and pressure indicator indium.

B. TF- μ SR experiments under pressure

The TF- μ SR signal collected under hydrostatic pressure conditions were analyzed by separating it into the sample and the pressure cell contribution by the following functional form:

$$A(t) = A_0 P(t) = A_s P_s(t) + A_{bg} P_{bg}(t), \quad (1)$$

where A_s and A_{bg} are the initial asymmetry associated to sample and background (mainly pressure cell), respectively. The polarization functions $P_s(t)$ and $P_{bg}(t)$ are given by:

$$P_s(t) = \exp(-\sigma^2/2) \cos(\gamma_\mu B_{int} t + \phi), \quad (2)$$

and

$$P_{bg} = \exp(-\sigma_{bg}^2/2) \cos(\gamma_\mu B_{bg} t + \phi), \quad (3)$$

where $\gamma_\mu/2\pi = 135.53$ MHz/T is the muon gyromagnetic ratio. B_{int} and B_{bg} are the local fields sensed by the ensemble of muons stopped inside the sample and the pressure cell, respectively. ϕ is the initial phase of the muon-spin ensemble. The measured Gaussian relaxation rate associated with the sample $\sigma(T)$ is shown in Fig. S2. σ is comprised of two parts: a contribution from the flux-line lattice σ_{sc} , and a temperature-invariant depolarization rate of nuclear moments σ_{nm} . σ_{nm} is obtained by fitting a TF- μ SR spectra collected above T_c . σ_{sc} is then extracted by quadratically subtracting σ_{nm} from σ .

C. Pressure dependence of gaps

The pressure dependence of the gap values at 0 K, i.e. $\Delta_{0,1}(p)$ and $\Delta_{0,2}(p)$ obtained by fitting the penetration depth $\lambda^{-2}(T)$ to a multigap model, show similar trends with respect to pressure as both $T_c(p)$ and $\sigma_0(p)$. The maximum around p_{c1} is not as pronounced as for the latter parameters; however, the gap values jump significantly at the critical pressure p_{c2} .

* Electronic address: ritu.gupta@psi.ch; Equal contribution

† Electronic address: debarchandas.phy@gmail.com; Equal contribution

‡ Electronic address: hlei@ruc.edu.cn

§ Electronic address: hubertus.luetkens@psi.ch

¶ Electronic address: rustem.khasanov@psi.ch

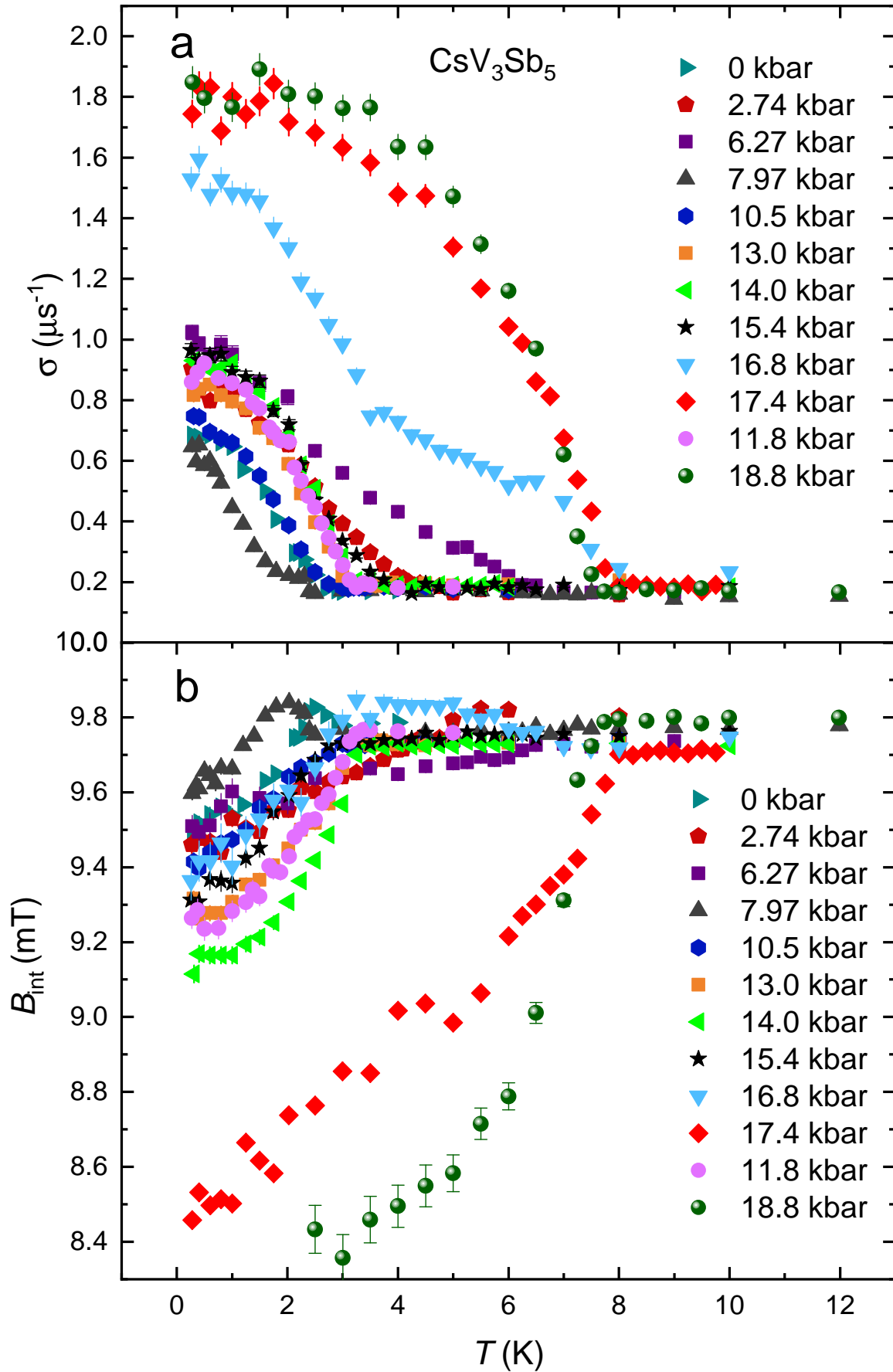


FIG. S2: a.) Measured Gaussian relaxation rate as a function of temperature $\sigma(T)$ for various pressures mentioned in the figure. b.) Temperature-dependent internal magnetic field $B_{\text{int}}(T)$ of the sample as sensed by the muons for the corresponding pressures in a.

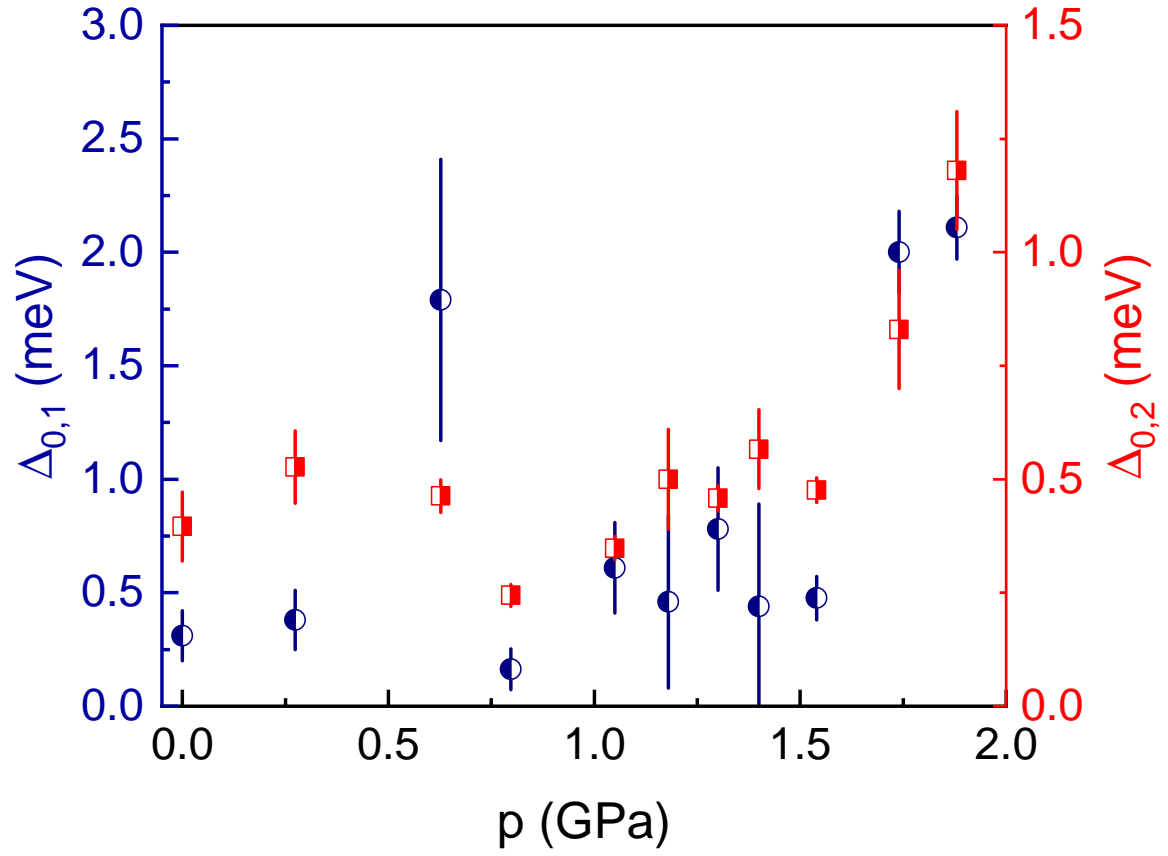


FIG. S3: Pressure variation of gap values $\Delta_{0,1}(p)$ and $\Delta_{0,2}(p)$, obtained from the multigap model fitting as described in the main text.